Dynamics and rheology of a suspension of super-paramagnetic chains under the combined effect of a shear flow and a rotating magnetic field

Emanuele Rossi,[1, a)] Jose A. Ruiz-Lopez,[1, b)] A.Vazquez-Quesada,[2, c)] and M. Ellero[1, 3, 4, d)]

[1)] *Basque Center for Applied Mathematics (BCAM), Alameda de Mazarredo 14, 48009 Bilbao, Spain*

[2)] *Department of Physics and Mathematics, Universidad de Alcalá, 28801 - Alcalá de Henares (Madrid), Spain*

[3)] *IKERBASQUE, Basque Foundation for Science, Calle de María Díaz de Haro 3, 48013 Bilbao, Spain*

[4)] *Zienkiewicz Centre for Computational Engineering (ZCCE), Swansea University, Swansea SA1 8EN, UK*

This study presents an analysis of the dynamics of a single and multiple chains of spherical super-paramagnetic beads suspended in a Newtonian fluid under the combined effect of an external rotating magnetic field and a shear flow. Viscosity results depend on two main non-dimensional numbers: the ratio between the shear rate and the magnetic rotation frequency and the ratio between the hydrodynamic and magnetostatic interactions (the Mason number). When the shear rate is smaller than the magnetic frequency, the chain rotation accelerates the surrounding fluid, reducing the value of the measured suspension viscosity even below the solvent one. In this regime, shear-thickening is observed. For values of the shear rates comparable to the rotation magnetic frequency, the viscosity reaches a maximum and non-linear coupling effects come up. If the shear rate is increased to values above the rotation frequency, the viscosity decreases and a mild shear-thinning is observed. In terms of the Mason number, the suspension viscosity reduces in line with literature results reported for fixed magnetic fields, whereas the shear-rate/magnetic-frequency ratio parameters induces a shift of the viscosity curve towards larger values. Results at larger concentrations and multiple chains amplify the observed effects.

[a)]Electronic mail: erossi@bcamath.org

[b)]Electronic mail: jaruiz@bcamath.org

[c)]Electronic mail: adolfo.vazquez@uah.es

[d)]Electronic mail: mellero@bcamath.org

I. INTRODUCTION

Complex fluids have been very promising in the last decades for their unique and versatile properties: polymer solutions, suspensions, active matter, etc[1]. Among complex fluids, suspensions with magnetically-active particles have developed an outstanding performance for their capability to tune their rheological properties upon the application of an external magnetic field.[2]

When a magnetic field is applied, magnetic particles in a suspension magnetise and form chain-like structures along the direction of the magnetic field. The morphology of these aggregates and the kinetics of aggregation are controlled by the magnetic field strength and the particle concentration.[3,4] Usually, these aggregates are not in thermodynamic equilibrium as the structure is kinetically trapped in metastable states.[5] Also, these chain-like aggregates typically gap-span. The structure formation of these gap-spanning aggregates has been studied in simulations[6–9] and it has also been observed experimentally with microscopic[10–12] and X-ray techniques.[13].

The flow properties of these suspensions change dramatically, leading to viscosity increase, and it is possible to tune their rheology simply by changing the magnetic field. If the suspension is subjected to a flow, the chain-like aggregates deform and can eventually break.[2,14] The use of magnetically-active materials with the appropriate rheological, physical or chemical properties has been extremely demanded by different industries from vibration control[15,16] to biomedical applications.[17]

From a dimensional analysis, it is possible to obtain non-dimensional numbers controlling the rheology of suspensions with magnetic particles. Generally speaking, the bulk rheological properties of suspensions of super-paramagnetic particles can be simplified by thermal energy, magnetic and hydrodynamic interactions, neglecting inertia.[18] The so-called lambda ratio is defined as the ratio between the magnetic energy and the thermal energy: $\lambda = U_m/k_B T$ where U_m is the magnetic energy between the paramagnetic particles strongly depending on the particle size, k_B is the Boltzmann constant and T is the temperature of the system. When the particle diameter is small and the thermal fluctuations are important (i.e. for ferrofluids), the viscosity increases mildly in the so-called magneto-viscous effect.[19,20] However, if the particle diameter and the magnetic field strength are large enough, and, thus, the lambda ratio is very high, $\lambda \gg 1$, thermal fluctuations can be neglected, the viscosity

increases dramatically and the suspension might show a yield stress. Those suspensions are named magneto-rheological (MR) fluids.[2,21] In this paper, we address the non-colloidal limit, neglecting the thermal interactions.

In the presence of flow, another dimensionless number can be defined as the ratio between the hydrodynamic and the magnetic forces: the Mason number, $Mn = F_{hyd}/F_0$,[18,22] where F_{hyd} is the hydrodynamic force and F_0 is the magnetic force. Conventionally, it has been defined considering single particle Stokes' drag for the hydrodynamic contribution, $F_{hyd} = 6\pi\eta_0 a^2 \dot{\gamma}$ and the dipolar magnetic force between two particles $F_0 = \frac{3\mu_0}{4\pi}\frac{m_0^2}{a^4}$, $Mn = 6\pi\eta_0 a^2\dot{\gamma}/F_0$. Here, η_0 is the solvent viscosity, $\dot{\gamma}$ is the shear rate (or the generalised flow rate in the case of non-shearing flows), μ_0 is the vacuum magnetic permeability, m_0 is the magnetic dipole of one particle and a is the particle radius.

In a simple shear experiment, when the particle concentration ϕ and the magnetic field strength H_0 are high enough, the suspension shows a yield stress behaviour and the viscosity diminishes as a function of the shear rate due to the deformation and breakup of the magnetic-particle chains that had been formed.[2] Also if the magnetic field strength increases, the viscosity increases.[23] In spite of this rich rheological response, if we represent the viscosity as a function of the Mason number, all curves at different magnetic fields collapse on a master curve.[22,24] Mason number usually considers dipolar magnetic interactions for dilute systems and in the linear magnetic regime, but some corrections with the mean magnetization approximation can be included for higher concentrations and near magnetic field saturation.[18]. It is important to note that, as it is possible to obtain a master curve as a function of the Mason number, and the Mason number only includes the dipolar interactions, multipolar interactions between particles can generally be neglected to provide a simple but effective model of the system.

The yield stress, and the transition from the magnetic-dominated regime to the hydrodynamic-dominated regime is thus only a function of the particle concentration.[2,24]. Micromechanical models have been proposed [e.g. Martin and Anderson (1996)[25], Volkova $et\ al.$ (2000)[26]] for dilute systems reporting a linear dependence on the concentration as the interaction between different chains is negligible. All these micromechanical models have been successfully used in the description of experimental studies for dilute suspensions. Thus, it is possible to model dilute MR fluids by only knowing the dynamics of a single chain and then extrapolate the results for a multiple-chain system.

When applying a rotating magnetic field, magnetic-active fluids exhibit very interesting structural properties. When the field-rotation frequency is slow enough, the magnetic chains rotate along the field direction. However, when the frequency increases, the chain rotation is not longer syncronised with the field rotation and eventually chain breakup occurs.[27–29] Also, it has been experimentally shown that, if the frequency of the rotating field is very high, chains show a 'jerky' motion and move forward and backward and then break [i.e. see Fig. 1 in Helgesen *et al.* (1990)[30]]. The critical breakup frequency has been obtained experimentally[28] and also predicted theoretically depending on the number of particles in the chain, $\omega_c \sim 1/N^2$, or $\omega \sim \log(N)/N^2$.[28,31,32] Furthermore, simulations using lubrication and the Smoothed Particle Hydrodynamic (SPH) method have been used to study the structure and dynamics of magnetic beads in a rotating field, showing results in good agreement with theoretical models with high-order lubrication corrections included.[29]

Mason number has also been defined in the case of rotation, $Mn_r = 192\pi\eta\omega a^2/F_0$[33]. Thus, as the rotational Mason number is proportional to the rotation frequency, the maximum number of particles that can be in a chain at a fixed Mason number would be related with the Mason number as $N_{max} \sim Mn_r^{-2}$.[27,33] This result is similar to theoretical results in micromechanical models for steady shear [see Eq. 9 in Martin and Anderson (1996)[25]]. It is important to note that, for a fixed concentration ϕ, when a shear rate is superimposed to a rotating magnetic field, there are only two independent dimensionless numbers governing the system: the ratio between the shear rate and the rotation frequency of the magnetic field, $\dot{\gamma}/\omega_H$ and the Mason number. The rotational Mason number can be obtained as a function of the other two, $Mn_r = 32\left(\frac{\omega_H}{\dot{\gamma}}\right) Mn$.

Moreover, the application of a rotating magnetic field has been reported to be important for several applications in literature such as magnetophoresis, providing an enhanced response in the presence of rotation.[34]

In a previous work[29] the case of a rotating field without shear was studied. Here, we aim at studying the rheological properties of a dilute suspension of paramagnetic particles under the combined effect of a shear flow and an externally imposed rotating magnetic field. In this paper, the dynamic and the rheological properties of this system are addressed using numerical simulations, considering short-range lubrication forces and the SPH method to model the many-body long-range hydrodynamic interactions. It is important to note that the explicit solvent and hydrodynamic interactions have scarcely been studied in the pre-

vious literature for MR fluids. In a recent paper[35], the authors have studied the rheology of MR fluids performing simulations using SPH. Results differed from typical Stokes' drag simulations in the total hydrodynamic stress computed (the Stokes' drag simulations overestimated it) but not in the prediction of the shear-thinning transition. When applying a shear rate in a magnetic suspension with a rotating field; the structural, dynamic and rheological properties of the system will depend in a complex way on their interplay and this effect will be investigated in detail in this paper.

This article is structured as follows: the SPH model is introduced in Sec. II where the short-range lubrication forces between rigid beads are also discussed. Interparticle magnetic forces are presented in Sec. III. The numerical parameters and the results are shown in Sec. IV and finally conclusions are reported in Sec. V.

II. SPH MODEL

In this section the SPH method used to run the simulations will be presented. The method description will be divided in different subsections, as follow: in Sec. II A details of the solvent medium will be given, in Sec. II B the suspended solid particles will be described and in Sec. II C the lubrication interactions will be discussed.

A. Suspending Newtonian fluid

The SPH method is a meshless Lagrangian model, in which the Navier-Stokes equations describing a Newtonian fluid are discretized by a set of points called fluid particles. Positions and momenta of every fluid particle evolve according to the following equations:[36]

$$\dot{\boldsymbol{r}}_i = \boldsymbol{v}_i$$

$$m\dot{\boldsymbol{v}}_i = -\sum_j \left[\frac{P_i}{d_i^2} + \frac{P_j}{d_j^2} \right] \frac{\partial W(r_{ij})}{\partial r_{ij}} \boldsymbol{e}_{ij} + \tag{1}$$

$$+ \sum_j (D+2)\eta_0 \left[\frac{1}{d_i^2} + \frac{1}{d_j^2} \right] \frac{\partial W(r_{ij})}{\partial r_{ij}} \frac{\boldsymbol{e}_{ij} \cdot \boldsymbol{v}_{ij}}{r_{ij}} \boldsymbol{e}_{ij}$$

where m is the fluid particle mass, $i = 1, .., N_{SPH}$ is the fluid particle index, D is the number of dimensions of the system, P_i the pressure of particle i, $\boldsymbol{e}_{ij} = \boldsymbol{r}_{ij}/r_{ij}$ the unit vector

joining particles i and j and $\boldsymbol{v}_{ij} = \boldsymbol{v}_i - \boldsymbol{v}_j$ their velocity difference. $d_i = \sum_j W(r_{ij}, r_{cut})$ is the number density of particle i estimated as a weighted interpolation with kernel function W with compact support r_{cut}[37]. η_0 is the fluid viscosity. Using this definition, continuity equation for the mass density $\rho_i = m d_i$ is automatically satisfied. The Newton's equations of motion Eq. (1) are a discrete representation of the momentum Navier-Stokes equation in a Lagrangian framework: the first summation in Eq. (1) is the pressure gradient term and the second the Laplacian of the velocity field. A quintic spline kernel[38] with cutoff radius $r_{cut} = 3\,\Delta r$, where Δr is the mean fluid particle separation, is used for the the weighting function W[39].

The following equation of state is used:

$$P_i = p_0 \left[\left(\frac{\rho_i}{\rho_{ref}} \right)^\gamma - 1 \right] \tag{2}$$

where $\rho_{ref} = 0.99\rho_0$ ensures a positive pressure and the input parameters ρ_0, p_0 and γ are chosen to have a speed of sound $c_s = \sqrt{\gamma p_0 / \rho_0}$ larger than any other velocity present in the problem to enforce approximate incompressibility[40].

B.   Solid particles: fluid-structure interaction

Solid bodies of arbitrary shape can be modelled using boundary particles similar to fluid ones.[41] Boundary particles, located inside the solid region, interact with fluid particles through the SPH forces described in Eq. (1). The presence of a solid body within the flow field requires the enforcement of the no-slip boundary conditions at the liquid-solid interface: during each time step an artificial velocity is assigned to the boundary particles satisfying zero interpolation at the interface.[38] The same approach is also used to model any arbitrary external wall.

The total SPH force $\boldsymbol{F}_\alpha^{\mathrm{sph}}$ and torque $\boldsymbol{T}_\alpha^{\mathrm{sph}}$ acting on solid particle α can then be evaluated in the following way

$$\boldsymbol{F}_\alpha^{\mathrm{sph}} = \sum_{j \in \alpha} \boldsymbol{F}_j, \qquad \boldsymbol{T}_\alpha^{\mathrm{sph}} = \sum_{j \in \alpha} (\boldsymbol{r_j} - \boldsymbol{R}_\alpha) \times \boldsymbol{F}_j \tag{3}$$

where $\boldsymbol{F}_j$ is the force and $\boldsymbol{r_j}$ the position of the boundary particle j and $\boldsymbol{R}_\alpha$ is the center of mass of the solid particle α. Solid particle's position, linear velocity $\boldsymbol{V}_\alpha$ and angular velocity

$\mathbf{\Omega}_\alpha$ can be therefore obtained by integration of Eq. (3). Boundary particles positions are then updated using $\mathbf{V}_\alpha$ and $\mathbf{\Omega}_\alpha$ and assuming a rigid body motion[42]. In the following we assume that $\alpha = 1, .., N$, where N is the total number of solid beads suspended in the liquid.

C. Interparticle lubrication/repulsion

The present SPH scheme accurately evaluates the long-range hydrodynamic interactions (HIs) between solid particles.[41] However, as discussed in detail in literature,[42–44] when two solid particles (e.g. α and β) get very close to each other, the SPH model does not longer reproduce the HIs between them and, as a consequence, the short-range forces acting on the solid particles need to be corrected. In previous works[42–44] an analytical solution has been obtained in the limit of small sphere's separation, and the corresponding pairwise short-range HIs has been considered and superimposed to the far-field multi-body SPH HIs. The normal and tangential lubrication forces acting between couples of spheres read:[45]

$$\mathbf{F}_{\alpha\beta}^{\text{lub},n}(s) = f_{\alpha\beta}(s)\mathbf{V}_{\alpha\beta} \cdot \mathbf{e}_{\alpha\beta}\mathbf{e}_{\alpha\beta}$$

$$\tag{4}$$

$$\mathbf{F}_{\alpha\beta}^{\text{lub},t}(s) = g_{\alpha\beta}(s)\mathbf{V}_{\alpha\beta} \cdot (\mathbf{1} - \mathbf{e}_{\alpha\beta}\mathbf{e}_{\alpha\beta})$$

where $\mathbf{e}_{\alpha\beta} = \mathbf{R}_{\alpha\beta}/R_{\alpha\beta}$ is the unit vector joining the centers of mass of solid particles α and β, $\mathbf{R}_{\alpha\beta} = \mathbf{R}_\alpha - \mathbf{R}_\beta$, $R_{\alpha\beta} = |\mathbf{R}_{\alpha\beta}|$ its magnitude; $\mathbf{V}_{\alpha\beta}$ is their relative velocity and $s = R_{\alpha\beta} - (a_\alpha + a_\beta)$ is the distance between spheres surfaces. The scalar functions $f_{\alpha\beta}(s)$ and $g_{\alpha\beta}(s)$ are defined as

$$f_{\alpha\beta}(s) = -6\pi\eta \left[\left(\frac{a_\alpha a_\beta}{a_\alpha + a_\beta}\right)^2 \frac{1}{s} + a_\alpha \left(\frac{1 + 7\frac{a_\beta}{a_\alpha} + \left(\frac{a_\beta}{a_\alpha}\right)^2}{5\left(1 + \frac{a_\beta}{a_\alpha}\right)^3}\right) \ln\left(\frac{a_\alpha}{s}\right) \right]$$

$$\tag{5}$$

$$g_{\alpha\beta}(s) = -6\pi\eta a_\alpha \left[\frac{4\frac{a_\beta}{a_\alpha}\left(2 + \frac{a_\beta}{a_\alpha} + 2\left(\frac{a_\beta}{a_\alpha}\right)^2\right)}{15\left(1 + \frac{a_\beta}{a_\alpha}\right)^3} \right] \ln\left(\frac{a_\alpha}{s}\right)$$

where a_α and a_β are the sphere's radii (in this paper, we consider all particles have the same radius, $a_\alpha = a_\beta = a$). As discussed in previous works,[42–44] excellent agreement is obtained in the HIs description over the entire range of interparticle distances s. An accurate and

efficient semi-implicit time integration splitting scheme[46] for the short-range lubrication forces is used to stabilize and speed up the simulations.[43]

Finally, an additional short-range repulsive force is introduced to prevent particles overlap. This force mimic, for example, particle's surface roughness or other short-range interactions as the electrostatic one. The expression used for this force is the following.[47,48]

$$\boldsymbol{F}_{\alpha\beta}^{\text{rep}} = F^{\text{rep}} \frac{\tau e^{-\tau s}}{1 - e^{-\tau s}} \boldsymbol{e}_{\alpha\beta} \tag{6}$$

where τ^{-1} determines the interaction range and F^{rep} its magnitude. In this work $\tau^{-1} = 0.001a$ and $F^{rep} = 0.02115$ is adopted, corresponding to a nearly hard-sphere model.

III.   CHAIN DYNAMICS UNDER A ROTATING MAGNETIC FIELD: MATHEMATICAL MODEL

A spatially homogeneous rotating magnetic field of the form $\boldsymbol{H} = H_0(\cos(\omega_H t), 0, \sin(\omega_H t))$ is considered and the rotation takes place on the plane (x, z) with angular frequency ω_H. The most relevant forces involved in the chain rotation and shape are the magnetic torque of the two particles at both ends of the chain, and the drag force. The effect of the tangential lubrication force between beads, which becomes particularly relevant for short chains, is also considered.

When the suspended solid beads are super-paramagnetic, the presence of an external magnetic field $\mathbf{H}$ will induce a magnetic dipole moment. The alignment of the magnetic moment $\boldsymbol{m}_\alpha$ of a given solid bead α with the external magnetic field is fast enough that it can be considered as instantaneous, in such a way that:

$$\boldsymbol{m}_\alpha = \frac{V_c \chi}{\mu_0} \boldsymbol{H}_\alpha \tag{7}$$

where $V_c = 4\pi a^3 f/3$ is the volume of a paramagnetic bead of radius a, with f being the fraction of the bead's volume that is paramagnetic and $\boldsymbol{H}_\alpha$ the magnetic field estimated at the beads position $\boldsymbol{R}_\alpha$. χ is the magnetic susceptibility difference between the bead and the suspending fluid, whereas μ_0 is the vacuum magnetic permittivity. Eq. (7) is valid under the assumption that the external field $\boldsymbol{H}$ is not too large, in such a way that a linear regime is preserved.

As a result, the induced dipole-dipole magnetic force between two beads α and β can be expressed as[49]

$$\boldsymbol{F}_{\alpha\beta}^{B} = \frac{3\mu_0}{4\pi R_{\alpha\beta}^4} \left[\left(\boldsymbol{m}_\alpha \cdot \boldsymbol{e}_{\alpha\beta}\right) \boldsymbol{m}_\beta + \left(\boldsymbol{m}_\beta \cdot \boldsymbol{e}_{\alpha\beta}\right) \boldsymbol{m}_\alpha - \right.$$
$$\left. \left(5 \left(\boldsymbol{m}_\beta \cdot \boldsymbol{e}_{\alpha\beta}\right) \left(\boldsymbol{m}_\alpha \cdot \boldsymbol{e}_{\alpha\beta}\right) - \left(\boldsymbol{m}_\alpha \cdot \boldsymbol{m}_\beta\right)\right) \boldsymbol{e}_{\alpha\beta} \right] \tag{8}$$

In the case of identical solid particles and homogeneous magnetic field $\boldsymbol{H}$, each bead will have the same magnetic moment $\boldsymbol{m}_\alpha = \boldsymbol{m}_\beta = \boldsymbol{m}$ and Eq. (8) becomes:

$$\boldsymbol{F}_{\alpha\beta}^{B} = \frac{3\mu_0}{4\pi R_{\alpha\beta}^4} \left[2 \left(\boldsymbol{m} \cdot \boldsymbol{e}_{\alpha\beta}\right) \boldsymbol{m} - \left(5 \left(\boldsymbol{m} \cdot \boldsymbol{e}_{\alpha\beta}\right)^2 - m_0^2\right) \boldsymbol{e}_{\alpha\beta} \right] \tag{9}$$

Eq. (9) can be re-written in the following way:

$$\boldsymbol{F}_{\alpha\beta}^{B} = \frac{F_0}{\overline{R}_{\alpha\beta}^4} \left[2 \left(\overline{\boldsymbol{m}} \cdot \boldsymbol{e}_{\alpha\beta}\right) \overline{\boldsymbol{m}} - \left(5 \left(\overline{\boldsymbol{m}} \cdot \boldsymbol{e}_{\alpha\beta}\right)^2 - 1\right) \boldsymbol{e}_{\alpha\beta} \right] \tag{10}$$

where $\overline{\boldsymbol{m}} = \boldsymbol{m}/m_0$ and $\overline{R}_{\alpha\beta} = R_{\alpha\beta}/a$, $F_0 = \frac{3\mu_0}{4\pi} \frac{m_0^2}{a^4} = \frac{4\pi}{3\mu_0} \left(a f \chi H_0\right)^2$ and $m_0 = \frac{V_c \chi}{\mu_0} H_0$.

IV. NUMERICAL RESULTS

A. Numerical setup

A chain of seven paramagnetic spherical beads of radius a is suspended in a Newtonian fluid undergoing a shear flow in the xz plane, as shown in Fig. 1. In order to impose a uniform shear flow $\dot{\gamma}$, two rigid plates are considered in the planes normal to the $z-$direction, moving in opposite directions along the x-axis. The chain center bead is placed at the center of the computational domain, a cubic box of side $L = 25a$. This condition corresponds to an ultra-dilute suspension. Box size was always chosen so that the distance between the chain and the top and bottom walls in the z-direction is always larger than one particle radius to avoid wall effects. However, it is important to note that in typical simulations for magnetorheology and in experiments, chains do usually span along the whole gap between walls [e.g. Kittipoomwong *et al.* (1005), Liu *et al.* (2010), Peng *et al.* (2020), Zhang *et al.* (2020)].[6–9] This fact is also found in experiments with fixed magnetic fields and percolating structures has been seen by microscopy and X-ray techniques [e.g. Kor *et al.* (2020), Schumann *et al.* (2019)].[11,13] In order to compare with magnetorheological experiments and simulations with fixed magnetic fields, we kept a moderate separation between the top and

bottom parts of the chain and the walls, but the separation between the chain and the wall was always larger than a particle radius a to ensure a full resolution of the SPH model.

For all the simulations presented in this work the SPH resolution used is $\Delta r/a = 0.3$ where Δr is the mean particle spacing. The total number of SPH particles in this case is $N = 466893$. Note that the number of particles was chosen based on the validation made in our previous work[29]. The fluid viscosity and density are respectively $\eta_0 = 0.5$ and $\rho_f = 1.0$. The magnetic field is rotating in the same plane of shear xz and same direction. In order to avoid the break-up of the chain, the maximum angular frequency for the magnetic field was $\omega_H = 0.4\omega_c$, where ω_c is the critical angular frequency for chain break-up in absence of shear flow.[29] With this choice of ω_H the chain rotates as a nearly-rigid body under zero-flow conditions[29]. The imposed shear rates here vary between $\dot{\gamma}/\omega_H = 0.16$ and $\dot{\gamma}/\omega_H = 3.6$. The range of shear rates has been chosen in order to ensure a Reynolds number $Re = l^2\dot{\gamma}\rho_f/\eta_0 << 1$, where $l = 14a$ is the chain's length, and to minimize inertial effects. The Re numbers ranges from $Re = 2.24 \cdot 10^{-3}$ when $\dot{\gamma}/\omega_H = 0.16$ to $Re = 0.5$ when $\dot{\gamma}/\omega_H = 3.6$.

Periodic boundary conditions has been set in the x and y direction but not in the z-direction. This setup has been used extensively in magnetorheology [e.g. Klingenberg *et al.* (1989)[50], Mohebi *et al.* (1996)[51], Ly *et al.* (1999)[52], Heine *et al.* (2006)[53], Kor and See (2010)[11]]. One of the reasons for this choice is that periodic boundary conditions in the z-direction would lead to an infinite set of replicas in the z-direction, which would model magnetized walls instead of the experimental situation where non-magnetic plates are often used. Moreover, wall-based approaches to impose a shear flow have been rheologically validated in our previous works[42–44] .

B.   Rheology and dynamics: effect of $\dot{\gamma}/\omega_H$

The simulation results are displayed in Fig. 2 which shows the suspension viscosity η as a function of different applied shear rates $\dot{\gamma}$ by keeping the frequency ω_H of the rotating external magnetic field H constant, $\omega_H = 0.4\omega_c$. We are in the case where the frequency is much lower than the critical break-up frequency as reported in a previous work[29]. At these frequencies, the chain always follows the direction of the external magnetic field. The overall suspension viscosity is measured directly from the time averaged tangential force acting on
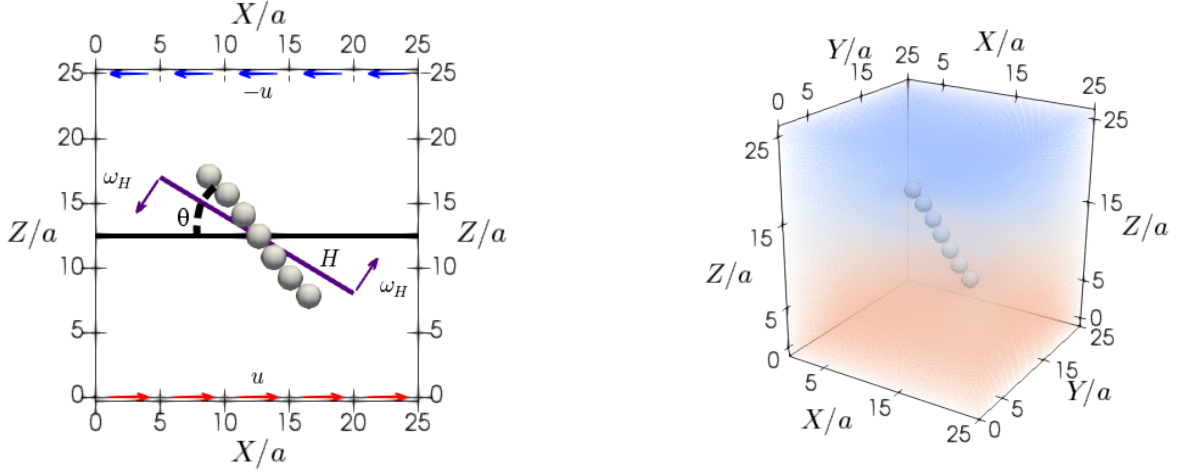
FIG. 1. Left: Scheme of computational set-up. The magnetic field $\mathbf{H}$ is rotating with angular frequency ω_H in the xz plane while the Newtonian fluid undergoes a shear flow. Right: full computational domain with the chain and SPH particles. The SPH particles are colored using their velocity component along the x-axis.

the walls, i.e.

$$\eta(\dot{\gamma}) = \frac{F_x}{A\dot{\gamma}}, \tag{11}$$

where A is the surface of the plates.

Fig. 2 shows a complex rheological behaviour including shear-thickening and thinning effects. At very low shear rates the suspension viscosity $\eta(\dot{\gamma})$ is lower than the matrix fluid viscosity η_0. By increasing the shear rate, a consequent increase of viscosity up to a constant value of about $\eta/\eta_0 = 1.06$ for values of $\dot{\gamma}/\omega_H \simeq 1.0$ is observed. Further increasing of the shear rate in the range $2.0 \leq \dot{\gamma}/\omega_H < 3.6$ leads to thinning in the viscosity, while for $\dot{\gamma}/\omega_H = 3.6$ the chain breaks up producing a sudden drop of the viscosity (not shown here).

To better explain this viscosity behaviour, the range of $\dot{\gamma}/\omega_H$ analysed will be divided in three regions: (i) shear thickening for $\dot{\gamma}/\omega_H \leq 0.6$, (ii) constant viscosity for $0.8 \leq \dot{\gamma}/\omega_H \leq 1.2$, (iii) shear thinning $2.0 \leq \dot{\gamma}/\omega_H < 3.6$. For each zone plots, the SPH particle non-dimensional velocities in direction parallel to the flow versus vertical coordinate z will be analysed, linking them to viscosity time evolution and to particular chain configurations.
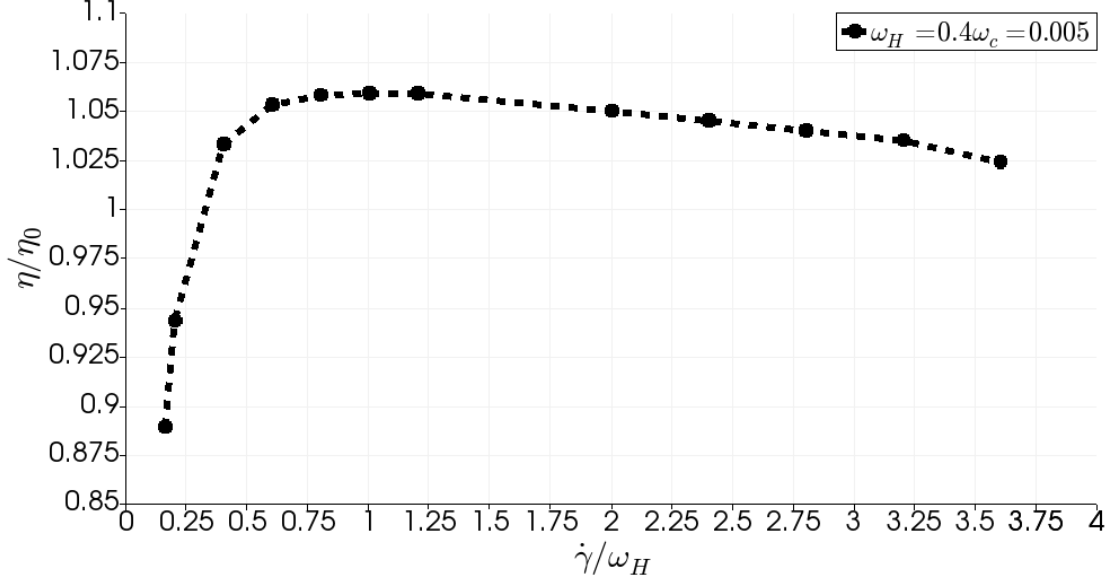
11

FIG. 2. Time-averaged non-dimensional viscosity η/η_0 vs $\dot{\gamma}/\omega_H$. Angular frequency ω_H of the rotating magnetic field was kept fixed in each case.

1. Shear thickening regime: $\dot{\gamma}/\omega_H \leq 0.6$

Fig. 3 shows the viscosity time evolution for $\dot{\gamma}/\omega_H \leq 0.6$. Note that, unlike results in Vazquez-Quesada *et al.* (2017),[29] where the motion of a single chain in an external rotational magnetic field was studied, here the chain's angular rotation does not reach a steady state but a periodic time-dependent modulation is superimposed in the presence of a shear flow. This leads to the periodicity in the measured viscosity (Fig. 3) and it is consistent with the rotational motion of elongated rigid objects in a simple uniform shear flow in the absence of inertial and Brownian forces[54]. For all the simulation reported in Fig. 3, i.e. for $\dot{\gamma}/\omega_H \leq 0.6$, the minimum corresponds to the chain being vertical in the xz plane while the maximum to the chain being horizontal (see discussion below).

It is possible to note that for this system at $\dot{\gamma}/\omega_H = 0.16$ and $\dot{\gamma}/\omega_H = 0.2$ the non-dimensional suspension viscosity takes minimum values lower than one (in particular $(\eta/\eta_0)_{min} = 0.6$ for $\dot{\gamma}/\omega_H = 0.16$ and $(\eta/\eta_0)_{min} = 0.72$ for $\dot{\gamma}/\omega_H = 0.2$), leading to an effective dissipation smaller than the pure fluid matrix. This is a very interesting result since the introduction of solid particles in a fluid usually leads to a rise in the viscosity even in very dilute systems. However, in the present situation, the rotation of the chains in the direction of the shear rate forces the fluid to move faster with respect to the situation where

12

no field is applied or if the magnetic field is constant. Similar results have been recently reported by the application of rotational fields in magnetophoresis[34].

Moreover, by increasing the shear rate, whereas the local temporal minima of η increase monotonically, the maximum values remain nearly constant, with an approximate value of $(\eta/\eta_0)_{max} = 1.15$.
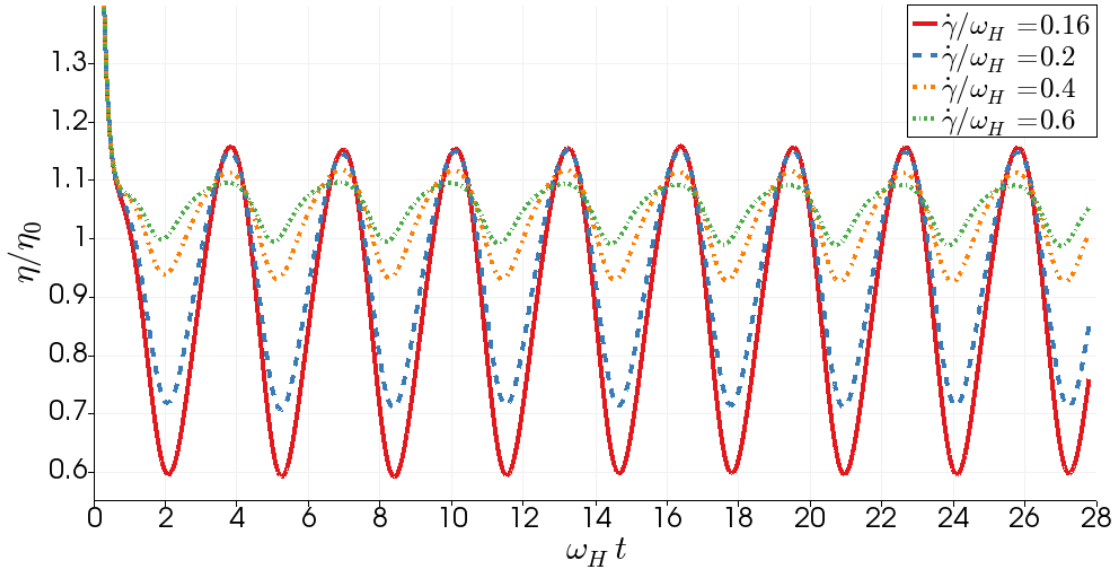

FIG. 3. Non-dimensional viscosity time evolution $\eta(t)/\eta_0$ for $\dot{\gamma}/\omega_H \leq 0.6$. Four complete periods of rotation shown.

It is possible to understand the viscosity behaviour by a detailed analysis of the transient flow field for different chain configurations. In particular, the case $\dot{\gamma}/\omega_H = 0.16$ will be analysed at three particular time instants, highlighted with black dots on Fig. 5. Fig. 6 depicts the chain configurations and related SPH particles non-dimensional velocities at the corresponding time instants. The x-axis of bottom row of Fig. 6 represents the SPH particles non-dimensional velocities in direction parallel to the flow, while the y-axis represents SPH particles vertical coordinate. Particles are classified in four different regions on the direction orthogonal to the plane of rotation. Each region is represented using different colors to highlight particles distance from the chain as described in Fig. 4. SPH velocity field close to the chain is depicted in black, whereas the field corresponding to regions far from the chain is marked in red.

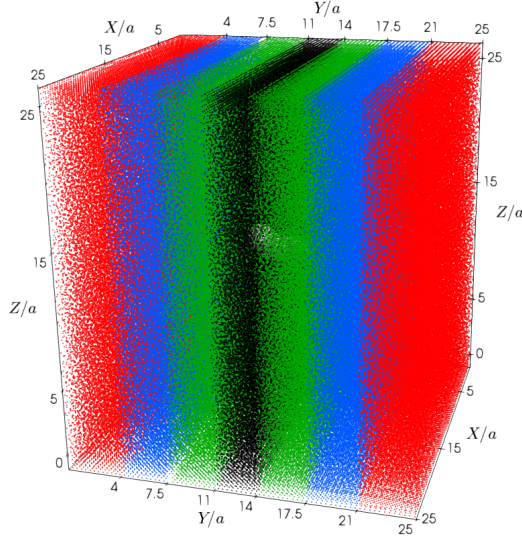For the case $\dot{\gamma}/\omega_H = 0.16$, when η/η_0 reaches its minimum value (points 1 and 3 of Fig. 5),

FIG. 4. Region subdivision of the flow field. Red: $y/R < 4 \cup y/R > 21$. Blue: $4 < y/R < 7.5 \cup 17.5 < y/r < 21$. Green: $7.5 < y/R < 11 \cup 14 < y/R < 17.5$. Black: $11 < y/r < 14$.

the chain is in a vertical configuration (see left and right top plots of Fig. 6). In this case, the chain velocity is higher than the velocity of the surrounding fluid and, as a consequence, the portions of fluid close to the chain are accelerated (with respect to the imposed shear flow at the given $\dot{\gamma}$). This, in turn, generates a velocity gradient near the wall smaller (or even opposite in sign) than the applied shear rate $\dot{\gamma}$. This results in an overall decrease of the measured suspension viscosity. Note that a change in sign of the velocity gradient should lead to a negative viscosity, however, this occurs only locally (in the part of the wall close to the chain; black/green points in Fig. 6), and therefore it is balanced by the normal applied shear rate (red points for regions far from the chain), leading globally to a simple viscosity reduction. The case of larger concentrations and multiple rotating chains leads to an amplification of this effect and it is discussed in the Sec. IV D and Sec. IV E.

When the chain is in a horizontal configuration (i.e. parallel to the wall: middle plots in Fig. 6), it is not able to modify appreciably the superimposed velocity gradient near the wall and, as a consequence, the viscosity reaches its maximum (point 2 in Fig. 5). The same behaviour could also be observed for the case $\dot{\gamma}/\omega_H = 0.2$.

The increase of the shear rate from $\dot{\gamma}/\omega_H = 0.2$ to $\dot{\gamma}/\omega_H = 0.4$ and $\dot{\gamma}/\omega_H = 0.6$ leads to changes in the maximum and minimum viscosity values. In particular the minimum values
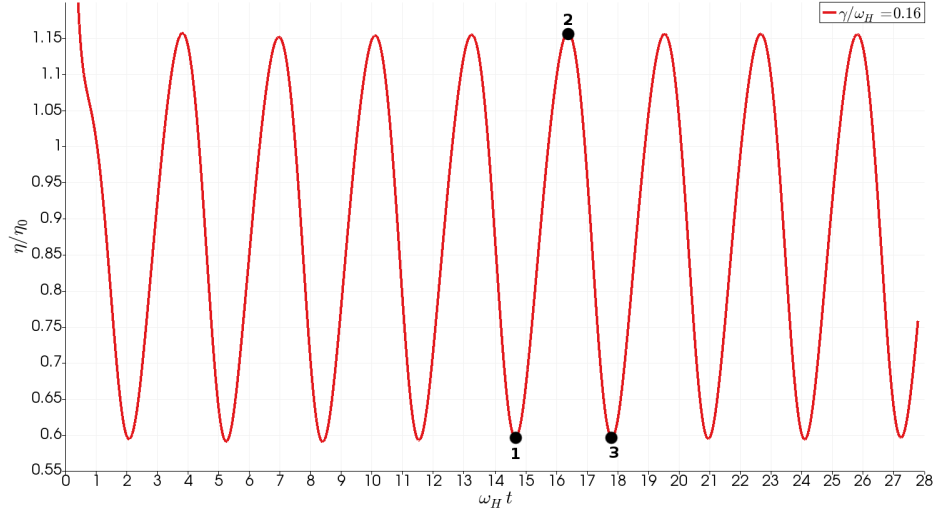
14

FIG. 5. η/η_0 time evolution for $\dot{\gamma}/\omega_H = 0.16$. Black dots denote particular chain configurations in the xz plane: in 1 and 3 the chain is vertical while in 2 is horizontal. Chain configurations and related SPH particles velocities are shown in Fig. 6

continue to rise significantly from $(\eta/\eta_0)_{min} = 0.93$ for $\dot{\gamma}/\omega_H = 0.4$ and $(\eta/\eta_0)_{min} = 0.99$ for $\dot{\gamma}/\omega_H = 0.6$, while the maximum values starts to decrease slightly being $(\eta/\eta_0)_{max} = 1.12$ for $\dot{\gamma}/\omega_H = 0.4$ and $(\eta/\eta_0)_{min} = 1.09$ for $\dot{\gamma}/\omega_H = 0.6$. Overall, the time-averaged viscosity increases accordingly to the shear-thickening reported in Fig. 2. The shape of the time evolution curve for the viscosity shows only minor changes moving from $\dot{\gamma}/\omega_H = 0.2$ to $\dot{\gamma}/\omega_H = 0.6$.

2.   *Constant viscosity regime:* $0.8 \leq \dot{\gamma}/\omega_H \leq 1.2$

Fig. 7 shows the viscosity time evolution of $\eta(t)/\eta_0$ for $0.8 \leq \dot{\gamma}/\omega_H \leq 1.2$. For all the simulations reported in Fig. 7, the minimum, as for the previous cases, corresponds to the chain being vertical in the xz plane.

It is also important to note that the general shape of the $\eta(t)/\eta_0$ curves is changing with respect to the cases at $\dot{\gamma}/\omega_H \leq 0.6$: for $\dot{\gamma}/\omega_H = 0.8$, the maximum is an almost flat and constant plateau while it is recovered for $\dot{\gamma}/\omega_H = 1.0$ and $\dot{\gamma}/\omega_H = 1.2$. A loss of symmetry in the chain dynamics is also clearly visible in Fig. 7, which is probably related to the strong non-linear coupling between the applied shear flow and the forced magnetic rotation when $\dot{\gamma}/\omega_H \approx 1$. This non-linear behaviour has been already seen in many experiments
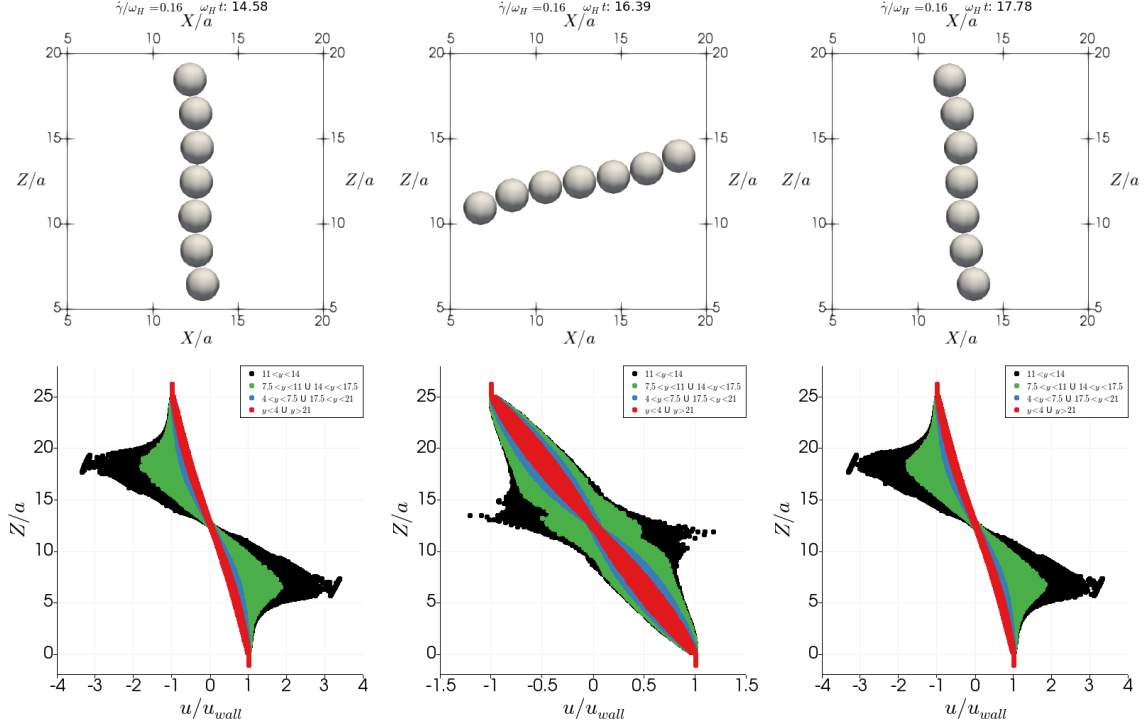
FIG. 6. Chain configurations and related SPH particles non-dimensional velocities at $\dot{\gamma}/\omega_H = 0.16$ for the time instant shown in Fig. 5: left 1, center 2, right 3.

and simulations in large-amplitude oscillatory shear (LAOS) flows[55,56] where, although in a different situation, the authors found a similar loss of symmetry on stress curves when the applied shear strain was higher than 5%.

Similarly to the previous section, for the case $\dot{\gamma}/\omega_H = 0.8$, when the chain is in a vertical configuration, $\eta(t)/\eta_0$ reaches its minimum value (see Supplementary information). Here, the chain velocity is only slightly higher than the surrounding fluid velocity (corresponding to the imposed linear profile), leading to a very small acceleration of the portion of fluid close to the chain. As a consequence, the modified velocity gradient near the wall is only moderately reduced. This leads to a small minimum in the $\eta(t)/\eta_0$ time behaviour only a 3% smaller than the mean value. When η/η_0 is almost constant, the chain has an angle with the horizontal xy-plane θ that varies between 27° and 0°. No particular asymmetry is observed.

For the case $\dot{\gamma}/\omega_H = 1.0$, when the chain is in vertical configuration, η/η_0 reaches its minimum value $\eta/\eta_0 = 1.03$ (see Supplementary information). In this case, the chain velocity is always very close to that of the surrounding fluid. This means that the chain is no longer
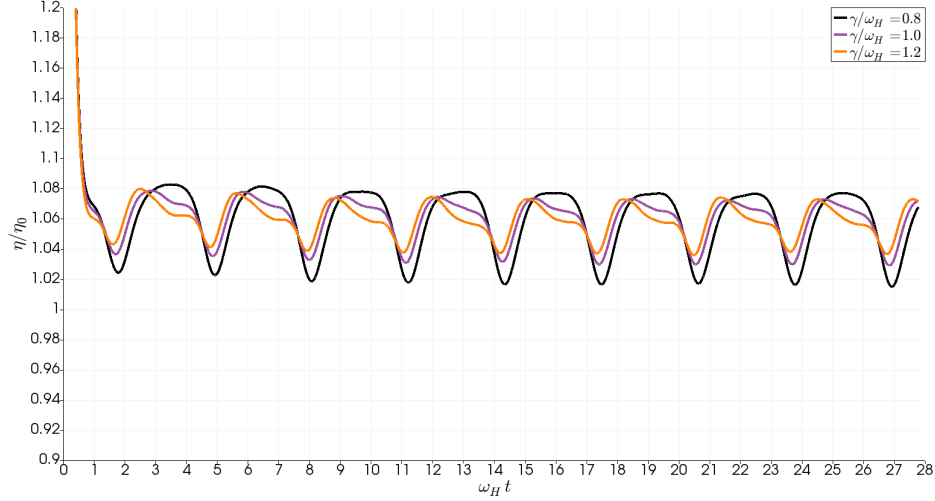
FIG. 7. Non-dimensional viscosity time evolution η/η_0 for $0.8 \leq \dot{\gamma}/\omega_H \leq 1.2$

accelerating the fluid.

It is interesting to note that, in this case, the maximum in the time evolution of η/η_0 no longer corresponds to an horizontal chain, as happened for the cases at $\eta/\eta_0 \leq 0.8$. In the current case the chain has an angle with the xy-plane, θ of about $34°$. This is the beginning of a change that will progressively bring the horizontal configuration to correspond to a minimum in the η/η_0 time behaviour whereas the maximum will correspond to configurations with higher θ-angle, as shown in plots of Fig. 8 and Fig. 10. In other words, when the shear rate is larger than the rotation frequency, the vertical configuration no longer accelerates the fluid particles near the wall as much as the shear rate does. Also, chains in a more vertical position begin to oppose to the shear-rate motion whereas the horizontal configuration shows the minimum resistance (a further explanation will be given in Sec. IV B 3). As the shear rate and the rotation frequency are very similar, some coupling between the motion modes with related non-linear effects could arise.[55,56]

3. *Shear thinning regime:* $\dot{\gamma}/\omega_H \geq 2.0$*:*

Fig. 8 shows the viscosity time evolution for $\dot{\gamma}/\omega_H \geq 2.0$. Unlike the previous cases, for all the simulations reported in Fig. 8 the local minima corresponds to the chain being placed always horizontally in the xy-plane.

Since the behaviour of the system is similar for all the simulations for $\dot{\gamma}/\omega_H \geq 2$, only
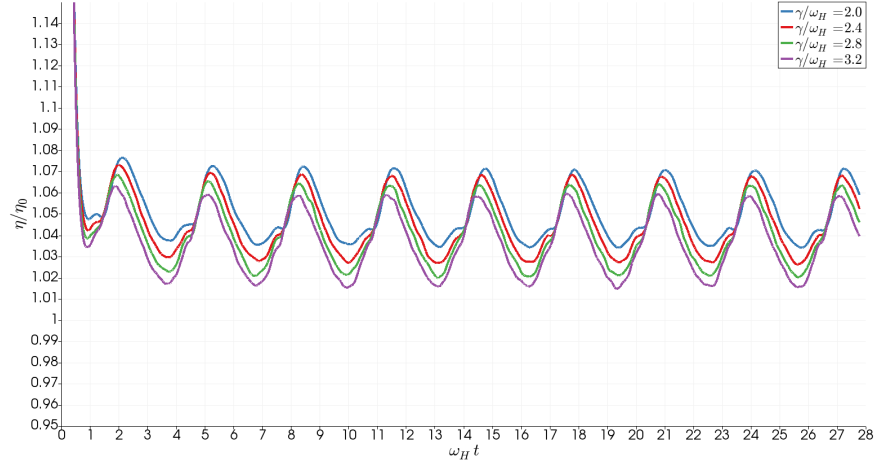
17

FIG. 8. Non-dimensional viscosity time evolution $\eta(t)/\eta_0$ for $\dot{\gamma}/\omega_H \geq 2.0$

the case $\dot{\gamma}/\omega_H = 2.0$ (shown in Fig. 9) will be analysed. In this case, η/η_0 does not reach anymore its minimum value when the chain is in vertical configuration: see points 1 and 5 of Fig. 9 and related configurations in Fig. 10 (top/bottom left plots). When $\dot{\gamma}/\omega_H \geq 2.0$, when the shear rate is larger than the rotation frequency, the chain in vertical position no longer accelerates the fluid particles, but it opposes a resistance to the motion, similar to what it happens in conventional magnetorheology for constant magnetic field [e.g. de Vicente et $al.$ (2011)[2]].

When η/η_0 reaches its maximum value $\eta/\eta_0 = 1.07$ (point 2), the chain has an θ-angle about 63°. This case is visible from the center-left bottom plot of Fig. 10 where the chain velocity is significantly lower with respect to that of the surrounding fluid and, as a consequence, the portions of fluid close to the chain are decelerated (with respect to the imposed shear flow), generating a velocity gradient near the wall larger than the shear rate. This results in a local temporal increase of the measured suspension viscosity. Thus, the maximum is not reached in the vertical position, but in a tilted position. This observation is also consistent with results from micromechanical models with fixed magnetic fields, where the critical angles where the stress was highest have been reported as $\theta = 48.2°,$[26] or $\theta = 50.8°.$[25]. However, it is important to note that the situation is not similar. The micromechanical models predicts an elastic deformation of the chains caused by the shear rate until it reaches a critical angle where the chain begins to break. Here, the chain rotates but the rotational frequency is always low and the chain would not break. The results from micromechanical models could explain why a tilted angle (with the shear plane) could lead to the highest
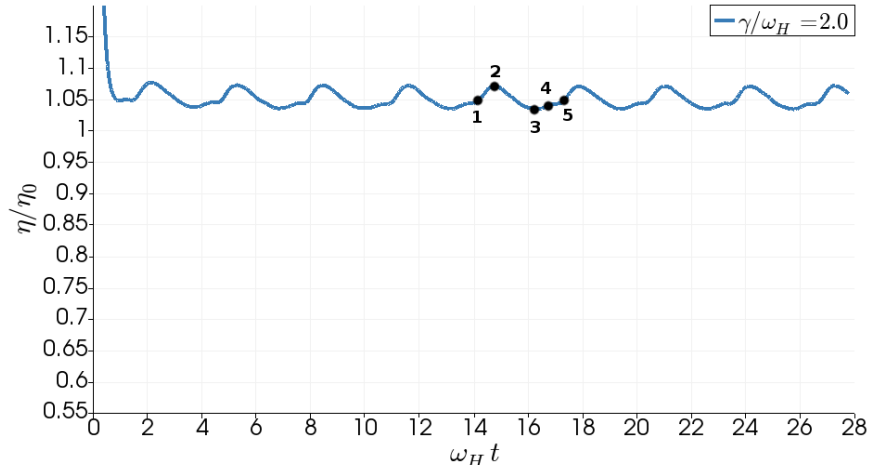
18

FIG. 9. η/η_0 time evolution for $\dot{\gamma}/\omega_H = 2.0$. Black dots denote particular chain configurations in the xz plane: in 1 and 5 the chain is vertical while it is horizontal in 3. Point 2 corresponds to the maximum while point 4 to an intermediate configuration. Chain configurations and related SPH particles velocities are shown in Fig. 10

stress but it is still not a critical situation where the chain is about to break and this could explain the differences between the angles.

When the chain is in an horizontal configuration, η/η_0 reaches its minimum value $\eta/\eta_0 = 1.035$, corresponding to point 3 of Fig. 9. This is consistent with the fact that, as shown in the center-right bottom plot of Fig. 10, the presence of the chain only minimally affects the velocity of the surrounding fluid as it does not longer oppose a resistance to the flow. Therefore, by increasing the applied shear rate from $\dot{\gamma}/\omega_H \leq 1.0$ to $\dot{\gamma}/\omega_H \gg 1.0$, the same instantaneous chain configuration affects in a different way the local temporal values of the corresponding measured viscosity.

It is also important to observe that in this regime the time-averaged values of the signals $\eta(t)/\eta_0$ displayed in Fig. 8 (i.e. right part of Fig. 2) show a mild linear decrease with a coefficient $m \approx -0.0125$. This shear-thinning behaviour is consistent with a scenario where chains are quasi-statically deforming in an external shear flow and it resembles the rheological results obtained for suspensions of aligned magnetic chains under a fixed external magnetic field.[2,18,22] It is important to note that, for $\dot{\gamma}/\omega_H \gg 1$, the applied shear rate increases, and, thus, the Mason number increases. Moreover, the magnetic field can be considered
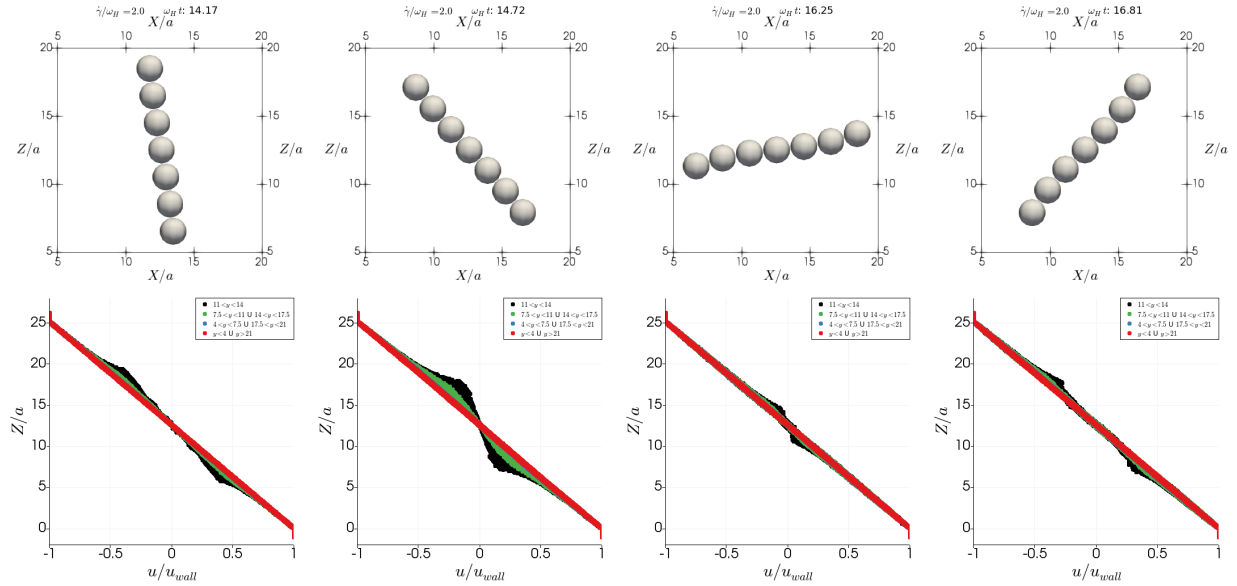
FIG. 10. Chain configurations and related SPH particles non-dimensional velocities for the time instant shown in Fig. 9: left 1 & 5, center-left 2, center-right 3, right 4

quasi-static with respect to the shear rate. This leads to the typical rheological behaviour reported in magnetorheology,[2,18,22] where shear thinning is observed in connection to the shear rate tending to deform and break the chains (see next section).

C.   Analysis of Mason number variation

As discussed in the Introduction, there are two major dimensionless numbers governing the rheological behaviour of this system: the ratio $\dot{\gamma}/\omega_H$ and the Mason number (note that, given these two numbers, the rotational Mason number is not a free parameter anymore). In the previous sections, the shear rate was increased whereas the rotation frequency remained constant (i.e. the rotational Mason number remained fixed). This case is very interesting for applications as the rotational field leads to different viscosity results from magnetorheology with fixed magnetic fields.[2,22]

Only at large $\dot{\gamma}/\omega_H$, where the shear-rate effect is more important, the typical shear-thinning behaviour obtained with fixed magnetic fields was observed. To better understand this situation, additional simulations were carried out. In these simulations, the ratio between the shear rate and the rotation frequency was kept constant, but the Mason number was varied (both the shear rate and the rotation frequency were changed keeping their ratio

constant but varying the Mason number).

Results are shown in Fig. 11. In this figure, the time-average non-dimensional viscosity is represented as a function of the Mason number at different $\dot{\gamma}/\omega_H$ corresponding to the cases discussed before. It should be noticed that, here, the Mason numbers explored were very low. However, it was not possible to increase further the Mason number without producing a breakup of the chain and therefore the range of Mn was limited by the critical breakup frequency ω_c which in turn depends the number of chain size as $Mn_{max} \sim 1/N^2$.[25,33] In any case, in a very dilute system, the transition between the magnetically-dominated to the hydrodynamically-dominated regime typically occur at very low Mason numbers.

For all the simulations performed here, the viscosity decreases with the Mason number. This result was expected as the hydrodynamic interactions tend to overcome the magnetic attraction and, as a result, to deform the structure reducing the viscosity.[2] In typical MR experiments with fixed magnetic field, viscosity reduces with a nearly-power-law trend with a slope close to -1 in a log-log scale.[2,22,57] After that, at some critical Mason number Mn^*, a transition occurs and the viscosity changes its trend leading to a leveling-off of the viscosity value close to the solvent viscosity.

Here, for the smallest value of $\dot{\gamma}/\omega_H$, the trend seems to be power-law (note the log-log scale in Fig. 11) at very low Mason numbers, in qualitative agreement with the experimental and theoretical results in magnetorheology with fixed magnetic fields. However, the time-average viscosity can become lower than the solvent viscosity, as explained in the previous sections. When the ratio $\dot{\gamma}/\omega_H$ increases, the power-law trend is not obtained anymore and the transition from the magnetically-dominated to the hydrodynamically-dominated regimes is qualitatively suggested. Also, the critical Mason number, Mn^* increases with the ratio $\dot{\gamma}/\omega_H$. This is a quite remarkable observation: as one of the main properties of MR fluids, the yield stress, is highly affected by the critical Mason number Mn^*,[24] the present results suggest that one possible way to control it, it is by actuating the MR fluid with a rotating magnetic field with a properly-tuned frequency. Also, it seems that the curves at high values of $\dot{\gamma}/\omega_H$ tend to converge. Since at these values of $\dot{\gamma}/\omega_H$, the shear rate is much higher than the rotation frequency, the situation would approach that for fixed magnetic field experiments (in steady shear).

From micromechanical models for fixed magnetic fields, it is possible to predict the viscosity curve as a function of the Mason number.[25] Martin and Anderson (1996) developed a
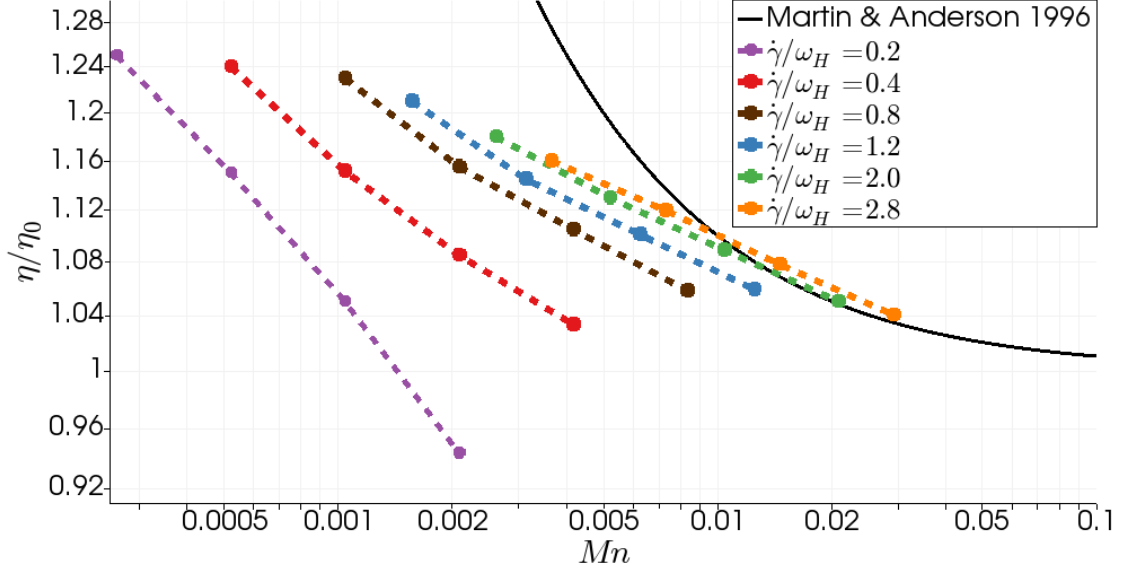
FIG. 11. Non-dimensional viscosity η/η_0 vs the steady shear Mason number, Mn, for different values of $\dot{\gamma}/\omega_H$. Black line represents the theoretical model curve from Martin and Anderson (1996):[25] $\eta/\eta_0 = 1 + Mn^*/Mn$ with $Mn^* = \frac{1}{5}\left(\frac{3}{2}\right)^{5/2}\phi \simeq 0.001$

micromechanical model based on torque balancing reporting that the system should follow a Bigham-like model: $\eta/\eta_\infty = 1 + Mn^*/Mn$. Here, η_∞ is the high-shear suspension viscosity and it is a function of the particle concentration. They also found that the critical Mason number only depends (linearly) on the particle concentration: $Mn^* = \frac{1}{5}\left(\frac{3}{2}\right)^{5/2}\phi$ [see Eqns. 13 and 14 in Martin and Anderson (1996)[25]]. Moreover, for highly dilute systems, the viscosity of the suspension can be well approximated by the solvent viscosity, i.e. $\eta_\infty \simeq \eta_0$. It is therefore possible to obtain a theoretical approximation of the viscosity curve for fixed magnetic fields by only knowing the concentration. The black solid line in Fig. 11 represents precisely the micromechanical model at the concentration explored. The simulation results at higher Mason number (and for the highest values of $\dot{\gamma}/\omega_H$) are very close to the theoretical approximation. In spite of this, simulation results at lower Mason numbers show viscosity values lower than the theoretical predictions for fixed magnetic fields. A possible explanation could lie in the fact that a rotating chain is in a continuous motion (even if slow), whereas for fixed magnetic fields, the fluid motion is completely blocked by the gap-spanning magnetic chains leading to the observed yielding behaviour. When the shear starts to deform the chains for fixed magnetic fields, the fluid motion is allowed and the results are

more comparable. This is a quite promising result since new rheological patterns emerge in these MR suspensions when an external rotating field is modulated.

D. Effect of the solid volume fraction ϕ

In this section three new simulations have been performed changing the domain size leading to a different volume fractions occupied by the beads $\phi = \frac{4\pi a^3 N}{3V}$, with N the total number of beads and V the computational domain volume. The parameters used for these simulations are displayed in Tab. I. All the simulations in this section have been performed using $\dot{\gamma}/\omega_H = 0.16$.

Simulation (a) is the same as that discussed in Sec. IV B 1 and it is reported here as a reference. The rest of the simulations (b), (c) and (d) have been performed reducing the domain size in order to increase ϕ as shown in Tab. I. The chain is always placed at the center of the computational domain.

Label	$\frac{L_x}{l}a \times \frac{L_y}{a} \times \frac{L_z}{a}$	ϕ	$\dot{\gamma}/\omega_H$
a	$25.0 \times 25.0 \times 25.0$	1.88^{-3}	0.16
b	$16.6 \times 25.0 \times 16.6$	4.25×10^{-3}	0.16
c	$16.6 \times 7.5 \times 16.6$	1.42×10^{-2}	0.16
d	$16.6 \times 5.0 \times 16.6$	2.12×10^{-2}	0.16

TABLE I. Simulations' parameters

Fig. 12 shows the viscosity time evolution for $\dot{\gamma}/\omega_H \leq 0.16$ and for the different domains described in Tab. I. For all the simulation reported in Fig. 12, the minimum corresponds to the chain being vertical in the xz plane while the maximum to the chain being horizontal.

From Fig. 12, it is possible to note that while the maximum of the $\eta(t)/\eta_0$ time evolutions for simulations (b), (c) and (d) remains close to that of simulation (a), the minimum decrease while increasing the solid volume fraction, resulting in an effective decrease of the mean (time-averaged) value of η/η_0. The decreasing trend is close to linear, as shown in Fig. 13, and it is in apparent contradiction with standard results in suspension rheology where an overall viscosity increase is observed for increasing ϕ (e.g. the linear Einstein's expression for the relative viscosity in the dilute limit). It must be however noticed that, in this case, the concentration of actively rotating chains is increased which, in turn, actuates on
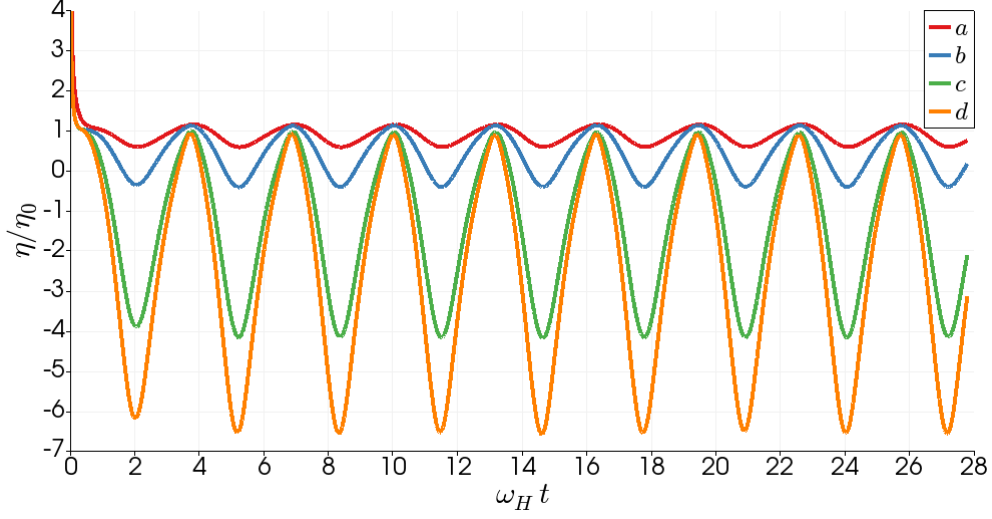
FIG. 12. Non-dimensional viscosity time evolution $\eta(t)/\eta_0$ for $\dot{\gamma}/\omega_H \leq 0.16$ and different volume fractions ϕ. Four complete periods of rotation shown.
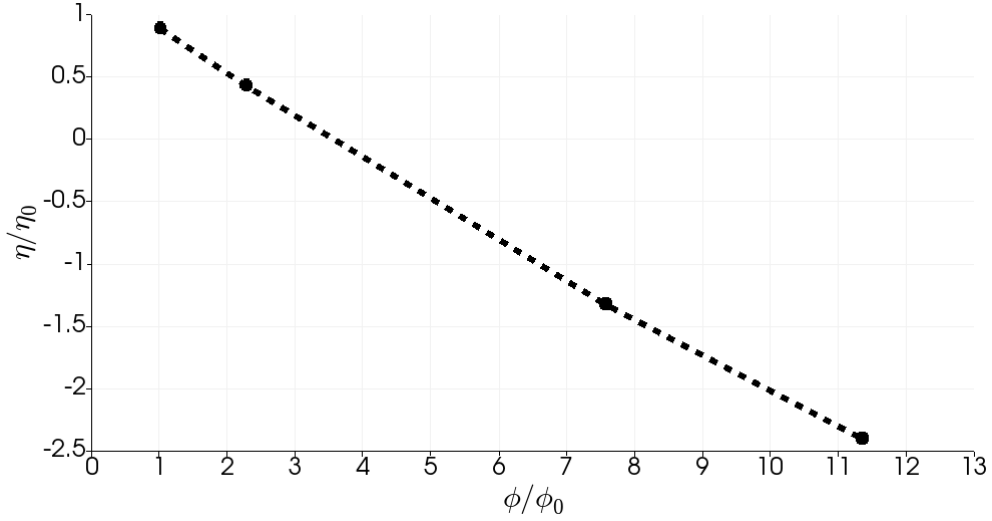

FIG. 13. Time averaged η/η_0 vs solid volume fraction for the simulations shown in Fig. 12. Letters refers to simulations labels of I. $\phi_0 \simeq 0.18\%$ is the solid volume fraction of case (a).

the surrounding fluid, leading to an amplification of the viscosity reduction effect already discussed in Sec. IV B 1.

Fig. 14 shows the velocity field for the two most extreme cases reported in Fig. 12: simulations (a) and (d). It can be seen that the fluid velocity field is mainly generated by the chain motion, and it increases in magnitude with the particle concentration. This motion accelerates elements of fluid close to the chain edges towards velocities larger than the wall
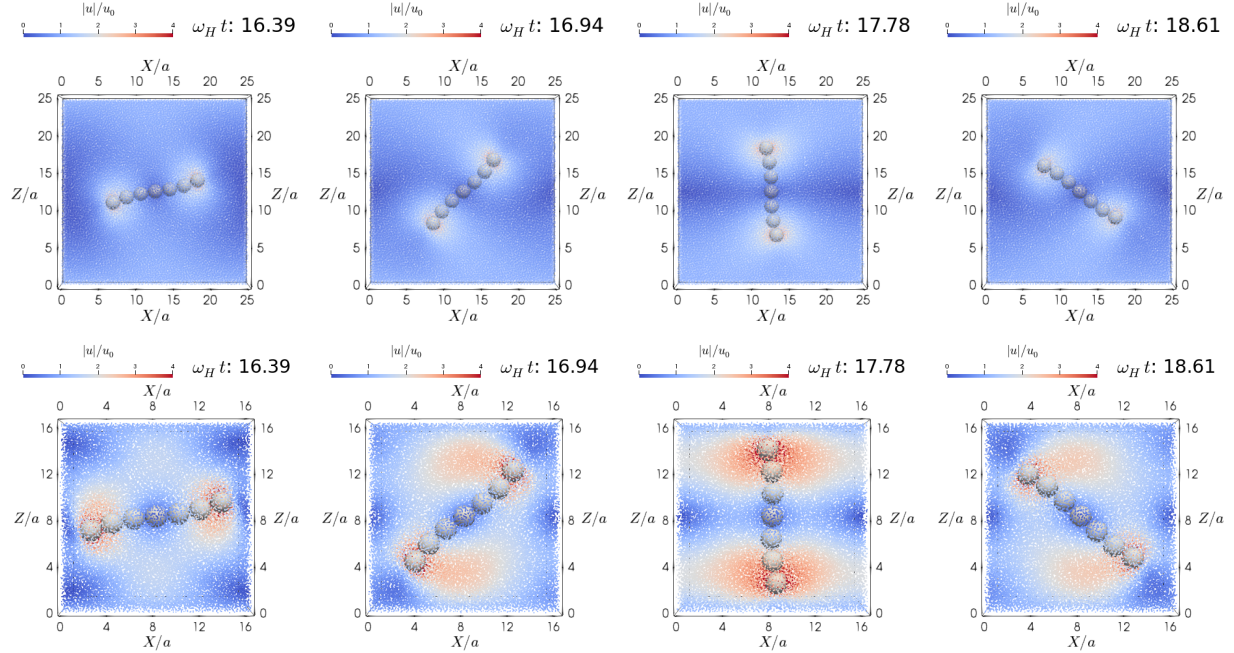
24

FIG. 14. SPH velocity fields for four different time instants. For the sake of brevity only simulations (a), first row, and (d), second row, are represented.

velocity, therefore generating an inverse velocity gradient and the related negative apparent viscosity discussed above. When chains are more concentrated, as seen in simulations (c) and (d), the coupled motion is able to change the sign of the stress leading to temporary negative values of the viscosity, especially when the chains are in vertical position and the spatial gap with the wall is small. This effect could be relevant in several technological applications, specially in the field of microfluidics, as rotating magnetic chains can be used as pumps generating flows or stirrers,[58] or valves with a fixed magnetic field where particle structures can be opposing to the flow rate and blocking gates in a microfluidics channel.[59]

E.   Multiple chains suspension

In the previous sections we have modelled the case of one single chain suspended in a fluid. In this section, a more realistic situation is considered with multiple chains. Chains were randomly distributed as represented in Fig. 15. The concentration was set exactly the same as in all the sections before [concentration (a) in the Sec. IV D]. All the simulations were performed for a ratio of the shear rate and the rotational frequency, $\dot{\gamma}/\omega_H = 0.16$. The

25

N_{chains}	$\frac{L_x}{a} \times \frac{L_y}{a} \times \frac{L_z}{a}$	N_{SPH}	η/η_0	σ_η
1	$25 \times 25 \times 25$	466893	0.888	0.001
4	$50 \times 50 \times 25$	1867443	0.889	0.004
16	$100 \times 100 \times 25$	7469903	0.891	0.006

TABLE II. Domain size and total SPH particles for the multimple chains simulations.

number of chains was varied from $N = 1$ (taken as a reference) up to $N = 16$. To ensure the same concentration, the box size was increased in the x and y-directions but not in the z-direction where the chains almost span the gap between walls. Also, the number of SPH particles increased in order to keep the same resolution, $\Delta r/a = 0.3$, up to $N_{SPH} = 7469903$ for the highest number of chains. The number of particles used in each simulation and the respective domain size are reported in Tab. II.
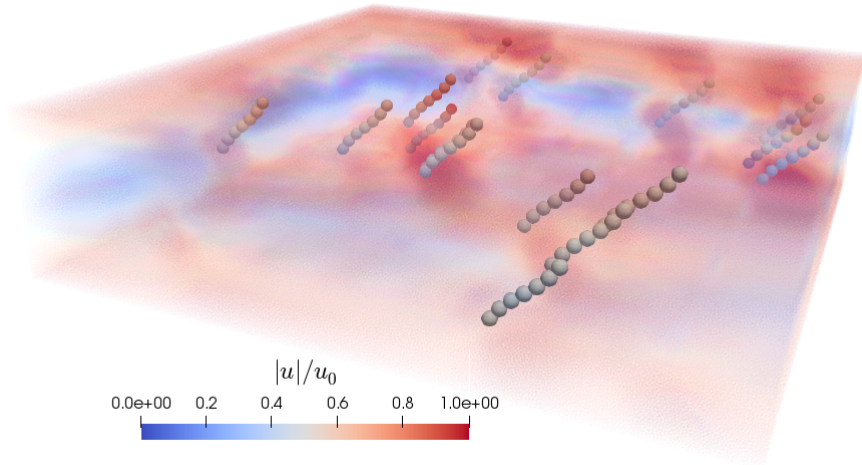

FIG. 15. Instantaneous SPH velocity field of the system with a number of chains $N_{chains} = 16$. Concentration was $\phi_0 \simeq 0.18\%$ and the ratio of the shear rate and the rotational frequency, $\dot{\gamma}/\omega_H = 0.16$. The scale maximum has been set to one for a better flow visualization.

For each chain set-up five different simulations were performed: in each simulation the chains where given a random initial position with the constrain of avoiding chain-chain and chain-walls interactions. The mean viscosity η was then evaluated averaging the one computed using Eq. (11) over the five different realizations. The mean viscosity η together with its standard deviation σ_η are reported in Tab. II and Fig. 16. It is important to note

that in this case the σ_η gives an estimate of the measured suspension viscosity variability due to different initial conditions. Looking at the obtained results this variability is always less then 1% meaning that the measured viscosity is not affected by chains initial positions.

As seen in Fig. 16 the results with multiple chains are very similar to the results with one single chain, provided that ϕ is the same. This rules out domain size effects and it is consistent with the assumption that, in the dilute case, the results with one chain are sufficiently accurate to represent a real system[25].
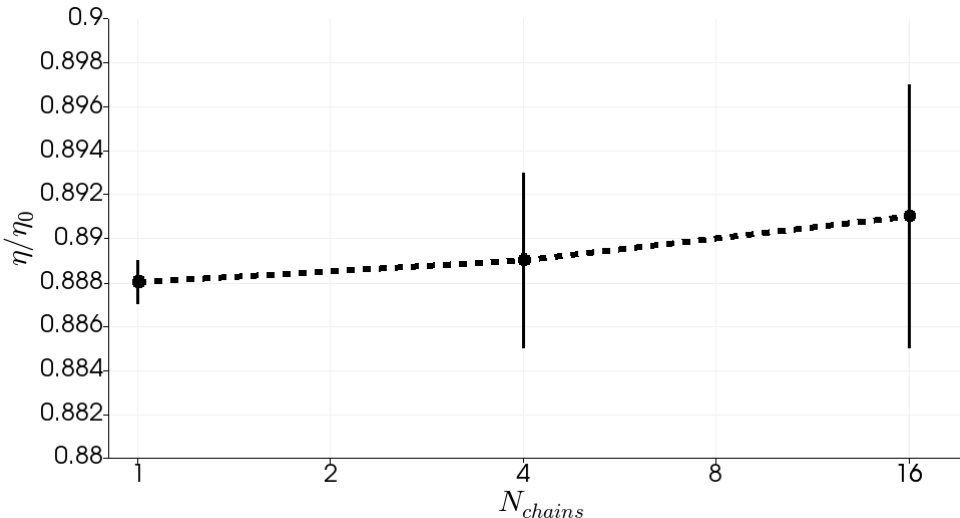

FIG. 16. Viscosity as a function of the number of chains in the system. Concentration was $\phi_0 \simeq 0.18\%$ and the ratio of the shear rate and the rotational frequency, $\dot{\gamma}/\omega_H = 0.16$. The vertical bars represents the standard deviations σ_η reported in Tab. II

V. CONCLUSIONS

In this work the dynamics of a single and multiple chains of spherical super-paramagnetic beads suspended in a Newtonian fluid under the combined effect of an external rotating magnetic field and a shear flow is investigated. The novel aspect introduced in this study is the combination of shear flow with a time-dependent (e.g. rotating) magnetic field and its effect on the resulting suspension rheology. Two non-dimensional numbers are governing the rheological behaviour of this system: the ratio between the shear rate and the rotation frequency, $\dot{\gamma}/\omega_H$, and the Mason number, Mn. When a rotating magnetic field is applied, the measured viscosity oscillates in time with a frequency related to the magnetic field rotation

27

frequency. Results obtained at low $\dot{\gamma}/\omega_H$ reveal that the time-average suspension viscosity shows a marked shear-thickening response and a (time-averaged) suspension viscosity that can be made lower than the fluid viscosity for small $\dot{\gamma}/\omega_H$. This effect can be significantly amplified at larger concentrations under the same flow conditions, leading to a sign-change in the measured viscous response.

When the factor $\dot{\gamma}/\omega_H$ increases, the viscosity reaches a maximum around $\dot{\gamma}/\omega_H \sim 1$ and then it starts to decrease. The latter shear-thinning effect occurring in the regime of moderate-to-large $\dot{\gamma}/\omega_H$, is similar to what generally observed in conventional magnetorheology using fixed magnetic fields. However, the critical Mason number (i.e. the transition from the magnetically-dominated to the hydrodynamic-dominated regimes) decreases with the ratio $\dot{\gamma}/\omega_H$.

VI. ACKNOWLEDGEMENTS

REFERENCES

[1] Deshpande AP, Krishnan JM, Kumar S, editors. Rheology of Complex Fluids. 1st ed. New York, NY: Springer New York; 2010.

[2] de Vicente J, Klingenberg DJ, Hidalgo-Alvarez R. Magnetorheological fluids: a review. Soft Matter. 2011;7(8):3701.

[3] Domínguez-García P, Melle S, Pastor JM, Rubio MA. Scaling in the aggregation dynamics of a magnetorheological fluid. Physical Review E - Statistical, Nonlinear, and Soft Matter Physics. 2007;76(5):1–13.

[4] Domínguez-García P, Melle S, Rubio MA. Morphology of anisotropic chains in a magnetorheological fluid during aggregation and disaggregation processes. Journal of Colloid and Interface Science. 2009;333(1):221–229.

[5]Swan JW, Vasquez PA, Whitson PA, Fincke EM, Wakata K, Magnus SH, et al. Multi-scale kinetics of a field-directed colloidal phase transition. Proceedings of the National Academy of Sciences of the United States of America. 2012;109(40):16023–16028.

[6]Kittipoomwong D, Klingenberg DJ, Ulicny JC. Dynamic yield stress enhancement in bidisperse magnetorheological fluids. Journal of Rheology. 2005;49(6):1521–1538.

[7]Liu T, Gu R, Gong X, Xuan S, Wu H, Zhang Z. Structural and rheological study of magnetic fluids using molecular dynamics. Magnetohydrodynamics. 2010;(3):257–270.

[8]Peng Y, Pei P. Microstructure evolution based particle chain model for shear yield stress of magnetorheological fluids. Journal of Intelligent Material Systems and Structures. 2020.

[9]Zhang J, Song W, Peng Z, Gao J, Wang N, Choi SB, et al. Microstructure simulation and constitutive modelling of magnetorheological fluids based on the hexagonal close-packed structure. Materials. 2020;13(7):1–19.

[10]Tang X, Zhang X, Tao R, Rong Y. Structure-enhanced yield stress of magnetorheological fluids. Journal of Applied Physics. 2000;87(5):2634–2638.

[11]Kor YK, See H. The electrorheological response of elongated particles. Rheologica Acta. 2010;49(7):741–756.

[12]Patel R. Mechanism of chain formation in nanofluid based MR fluids. Journal of Magnetism and Magnetic Materials. 2011;323(10):1360–1363.

[13]Schümann M, Gundermann T, Odenbach S. Microscopic investigation of the reasons for field-dependent changes in the properties of magnetic hybrid materials using X-ray microtomography. Archive of Applied Mechanics. 2019;89(1):77–89.

[14]Ilg P, Del Gado E. Non-linear response of dipolar colloidal gels to external fields. Soft Matter. 2011;7(1):163–171.

[15]Li WH, Du H. Design and experimental evaluation of a magnetorheological brake. International Journal of Advanced Manufacturing Technology. 2003;21(7):508–515.

[16]Zhu X, Jing X, Cheng L. Magnetorheological fluid dampers: A review on structure design and analysis. Journal of Intelligent Material Systems and Structures. 2012;23(8):839–873.

[17]Brusentsov NA, Nikitin LV, Brusentsova TN, Kuznetsov AA, Bayburtskiy FS, Shumakov LI, et al. Magnetic fluid hyperthermia of the mouse experimental tumor. Journal of Magnetism and Magnetic Materials. 2002;252(1-3 SPEC. ISS.):378–380.

[18]Ruiz-López JA, Fernández-Toledano JC, Hidalgo-Alvarez R, de Vicente J. Testing the mean magnetization approximation, dimensionless and scaling numbers in magnetorheol-

ogy. Soft Matter. 2016;12(5):1468–1476.

[19] Kröger M, Ilg P, Hess S. Magnetoviscous model fluids. Journal of Physics Condensed Matter. 2003;15(15).

[20] Rosensweig RE. Ferrohydrodynamics . Dover books on advanced mathematics. New York: Dover; 1997.

[21] Odenbach S, Thurm S. Magnetoviscous Effects in Ferrofluids Stefan. In: Lecture Notes in Physics; 2008. p. 185–201.

[22] Klingenberg DJ, Ulicny JC, Golden MA. Mason numbers for magnetorheology. Journal of Rheology. 2007;51(5):883–893.

[23] Bossis G, Lacis S, Meunier A, Volkova O. Magnetorheological fluids. Journal of Magnetism and Magnetic Materials. 2002;252:224–228.

[24] Ruiz-lópez JA, Hidalgo-alvarez R, Vicente JD. Towards a universal master curve in magnetorheology. Smart Materials and Structures. 2017;26(5):054001.

[25] Martin JE, Anderson RA. Chain model of electrorheology. J Chem Phys. 1996;104(12):4814–4827.

[26] Volkova, Bossis, Guyot, Bashtovoi, Reks. Magnetorheology of magnetic holes compared to magnetic particles. Journal Of Rheology. 2000;44(1):91–104.

[27] Melle S, Fuller GG, Rubio MA. Structure and dynamics of magnetorheological fluids in rotating magnetic fields. Physical Review E. 2000;61(4):4111–4117.

[28] Franke T, Schmid L, Weitz DA, Wixforth A. Magneto-mechanical mixing and manipulation of picoliter volumes in vesicles. Lab on a Chip. 2009;9(19):2831–2835.

[29] Vázquez-Quesada A, Franke T, Ellero M. Theory and simulation of the dynamics, deformation, and breakup of a chain of superparamagnetic beads under a rotating magnetic field. Physics of Fluids. 2017;29(3):032006.

[30] Helgesen G, Pieranski P, Skjeltorp AT. Nonlinear phenomena in systems of magnetic holes. Physical Review Letters. 1990;64(12):1425–1428.

[31] Gao Y, Hulsen MA, Kang TG, Den Toonder JMJ. Numerical and experimental study of a rotating magnetic particle chain in a viscous fluid. Physical Review E - Statistical, Nonlinear, and Soft Matter Physics. 2012;86(4):1–29.

[32] Petousis I, Homburg E, Derks R, Dietzel A. Transient behaviour of magnetic micro-bead chains rotating in a fluid by external fields. Lab on a Chip. 2007;7(12):1746–1751.

[33] Melle S, Calderón OG, Rubio MA, Fuller GG. Microstructure evolution in magnetorheological suspensions governed by Mason number. Physical Review E - Statistical Physics, Plasmas, Fluids, and Related Interdisciplinary Topics. 2003;68(4):1–11.

[34] Sherman ZM, Pallone JL, Erb RM, Swan JW. Enhanced diffusion and magnetophoresis of paramagnetic colloidal particles in rotating magnetic fields. Soft Matter. 2019;15(33):6677–6689.

[35] Lagger HG, Breinlinger T, Korvink JG, Moseler M, Di Renzo A, Di Maio F, et al. Influence of hydrodynamic drag model on shear stress in the simulation of magnetorheological fluids. Journal of Non-Newtonian Fluid Mechanics. 2015;218:16–26.

[36] Hu X, Adams N. Angular-momentum conservative smoothed particle dynamics for incompressible viscous flows. Physics of Fluids. 2006;18(10):101702.

[37] Español P, Revenga M. Smoothed dissipative particle dynamics. Physical Review E. 2003;67(2):026705.

[38] Morris JP, Fox PJ, Zhu Y. Modeling low Reynolds number incompressible flows using SPH. Journal of computational physics. 1997;136(1):214–226.

[39] Ellero M, Adams NA. SPH simulations of flow around a periodic array of cylinders confined in a channel. International Journal for Numerical Methods in Engineering. 2011;86(8):1027–1040.

[40] Monaghan JJ. Simulating free surface flows with SPH. Journal of computational physics. 1994;110(2):399–406.

[41] Bian X, Litvinov S, Qian R, Ellero M, Adams NA. Multiscale modeling of particle in suspension with smoothed dissipative particle dynamics. Physics of Fluids. 2012;24(1):012002.

[42] Vázquez-Quesada A, Bian X, Ellero M. Three-dimensional simulations of dilute and concentrated suspensions using smoothed particle hydrodynamics. Computational Particle Mechanics. 2016;3(2):167–178.

[43] Bian X, Ellero M. A splitting integration scheme for the SPH simulation of concentrated particle suspensions. Computer Physics Communications. 2014;185(1):53–62.

[44] Vázquez-Quesada A, Ellero M. Rheology and microstructure of non-colloidal suspensions under shear studied with Smoothed Particle Hydrodynamics. Journal of Non-Newtonian Fluid Mechanics. 2016;233:37–47.

[45] Kim S, Karrila SJ. Microhydrodynamics: principles and selected applications; 1991.

[46] Litvinov S, Ellero M, Hu X, Adams N. A splitting scheme for highly dissipative smoothed particle dynamics. Journal of Computational Physics. 2010;229(15):5457–5464.

[47] Dratler D, Schowalter W. Dynamic simulation of suspensions of non-Brownian hard spheres. Journal of Fluid Mechanics. 1996;325:53–77.

[48] Brady JF, Morris JF. Microstructure of strongly sheared suspensions and its impact on rheology and diffusion. Journal of Fluid Mechanics. 1997;348:103–139.

[49] Sing CE, Schmid L, Schneider MF, Franke T, Alexander-Katz A. Controlled surface-induced flows from the motion of self-assembled colloidal walkers. Proceedings of the National Academy of Sciences. 2010;107(2):535–540.

[50] Klingenberg DJ, van Swol F, Zukoski CF. Dynamic simulation of electrorheological suspensions. Journal of Chemical Physics. 1989;91(12):7888–7895.

[51] Mohebi M, Jamasbi N, Liu J. Simulation of the formation of nonequilibrium structures in magnetorheological fluids subject to an external magnetic field. Physical Review E - Statistical Physics, Plasmas, Fluids, and Related Interdisciplinary Topics. 1996;54(5):5407–5413.

[52] Ly HV, Reitich F, Jolly MR, Banks HT, Ito K. Simulations of Particle Dynamics in Magnetorheological Fluids. Journal of Computational Physics. 1999;155(1):160–177.

[53] Heine MC, de Vicente J, Klingenberg DJ. Thermal transport in sheared electro- and magnetorheological fluids. Physics of Fluids. 2006;18(2):1–11.

[54] Jeffery GB. The motion of ellipsoidal particles immersed in a viscous fluid. Proceedings of the Royal Society of London Series A, Containing papers of a mathematical and physical character. 1922;102(715):161–179.

[55] Hashemi MR, Manzari MT, Fatehi R. A SPH solver for simulating paramagnetic solid fluid interaction in the presence of an external magnetic field. Applied Mathematical Modelling. 2016;40(7-8):4341–4369.

[56] Li WH, Du H, Chen G, Yeo SH, Guo N. Nonlinear viscoelastic properties of MR fluids under large-amplitude-oscillatory-shear. Rheologica Acta. 2003;42(3):280–286.

[57] Ramos J, Klingenberg DJ, Hidalgo-Alvarez R, de Vicente J. Steady shear magnetorheology of inverse ferrofluids. Journal of Rheology. 2011;55(1):127–152.

[58] Pamme N. Magnetism and microfluidics. Lab on a Chip. 2006;6(1):24–38.

[59] Hatch A, Kamholz AE, Holman G, Yager P, Böhringer KF. A ferrofluidic magnetic micropump. Journal of Microelectromechanical Systems. 2001;10(2):215–221.